Article

Ionothermal Crystallization of SAPO-11 Using Novel Pyridinium Ionic Liquid and Its Catalytic Activity in Esterification of Levulinic Acid into Ethyl Levulinate

Al Issa Jehad Moh'dFathi Mohammad [1], Vinithaa Saminathan [1], Zeinhom M. El-Bahy [2], Laure Michelin [3,4], Tau Chuan Ling [5] and Eng-Poh Ng [1,*]

[1] School of Chemical Sciences, Universiti Sains Malaysia, Penang 11800, Malaysia
[2] Department of Chemistry, Faculty of Science, Al-Azhar University, Nasr City, Cairo 11884, Egypt
[3] Université de Haute-Alsace, Axe Matériaux à Porosités Contrôlées, Institut de Science de Matériaux de Mulhouse UMR 7361, ENSCMu, 3b rue Alfred Werner, 68093 Mulhouse, France
[4] Université de Strasbourg, 67000 Strasbourg, France
[5] Institute of Biological Sciences, Faculty of Science, University of Malaya, Kuala Lumpur 50603, Malaysia
* Correspondence: epng@usm.my

Abstract: A study using a novel pyridinium ionic liquid, namely 1-propylpyridinium bromide ([PPy]Br), to crystallize SAPO-11 under ionothermal conditions is reported. By carefully following the crystallization process, SAPO-11 can readily be crystallized in the presence of [PPy]Br, which serves as a synthesis solvent and structure-directing agent, at 150 °C after 133 h of heating. The study also focuses on manipulating other synthesis parameters (e.g., crystallization temperature, phosphorous content, silicon amount and [PPy]Br concentration) and investigating their respective effects on the formation of SAPO-11. The crystallized SAPO-11 has an acidic nature and a high surface area. Under conductive instant heating conditions, the SAPO-11 catalyst is very active in the conversion of levulinic acid into ethyl levulinate; 93.4% conversion and 100% selectivity of ethyl levulinate are recorded at 180 °C after 30 min of reaction. This result is comparable to or even better than those of conventional homogeneous catalysts.

Keywords: SAPO-11; ionothermal synthesis; catalyst; esterification; ethyl levulinate

1. Introduction

Zeolites are hydrated inorganic porous crystalline materials made up of interlinked tetrahedra of metal or nonmetal oxides (Si, Al or P). Among the zeolite family, aluminophosphates (AlPO-*n*) and silicoaluminophosphates (SAPO-*n*) are of particular interest, especially in petrochemical industries, due to their fascinating catalytic, ion exchange and separation properties [1,2]. In particular, SAPO-11 has well-aligned unidimensional elliptical pores of 4.0×6.5 Å^2 and is well suited for various chemical reactions, for instance, the hydroisomerization of *n*-paraffins [3], dewaxing [4], hydrodeoxygenation (HDO) of vegetable oils [5], *n*-alkane cracking [6] and oxidation of cyclohexane [7], thanks to its unique pore shape that leads to high product selectivity.

Classically, SAPO-11 can be crystallized via the hydrothermal route at 150–300 °C from reactive precursors containing amine or quaternary ammonium salts as organic structure-directing agents [8]. The presence of these organic species and the adjustment of synthesis conditions are important to ensure the formation of pure SAPO-11 with distinct morphological structures for task-specific applications [9–11]. Recently, an alternative route, the so-called ionothermal technique, for synthesizing zeolite materials has been reported [12–14]. Unlike the hydrothermal technique, this method uses a very polar ionic liquid instead of water as a nonaqueous solvent for transporting the inorganic reactants without interacting with the components in the ionogel, while concurrently also serving

as a structure-directing agent [15]. Due to using these nonvolatile solvents, the attributes of the ionothermal approach include the following distinct features: low or virtually no volatility, negligible vapor pressure, better thermal stability, tunable hydrophilibility and high reusability [16].

So far, imidazolium ionic liquids are the most commonly used in ionothermal synthesis for preparing SAPO-5 [17], MnAlPO-5 [18], SAPO34 [19], SAPO-LTA [20] and GaPO$_4$-LTA [21], while SAPO-11 can only be crystallized with the assistance of microwave heating [22]. Although various classes of ionic liquids (morpholinium, pyridinium, pyrrolidinium, piperidinium, imidazolium, etc.) have been synthesized [23–25], the ionothermal synthesis of SAPO-*n* zeolites is focused only on imidazolium-based ionic liquids. Hence, searching for ionic liquids other than imidazolium salts for crystallizing SAPO-*n* zeolites (e.g., SAPO-11) with unique surface and structural properties is of the utmost importance and worthy of further investigation.

Pyridinium ionic liquid is an ionic liquid containing a pyridinium cation. Compared with the imidazolium cation, the pyridinium cation is less polar due to the presence of only one N atom in its six-membered cyclic ring. In addition, the charge on the ring is fully localized, and hence, the coulomb and chemical interactions between the pyridinium cation and the counter anion are weaker than in the imidazolium based ionic liquid [26]. As a result, both features are expected to alter the crystallization profile of zeolites which indirectly affect the physicochemical properties of zeolite solids. To the best of our knowledge, no studies on the use of pyridinium ionic liquid for crystallizing zeolite materials under ionothermal conditions have been reported thus far.

In this study, SAPO-11 is crystallized with a new *N*-heterocyclic class of ionic liquid, namely 1-propylpyridinium bromide ([PPy]Br), in an ionothermal environment where the time-dependent study and effects of synthesis parameters (crystallization temperature, phosphorous content, silicon amount and [PPy]Br concentration) on the formation of SAPO-11 are investigated. Then, the prepared SAPO-11 is characterized before its catalytic behavior is studied in the esterification of levulinic acid and ethanol under conductive instant heating conditions that mimic rapid microwave heating.

2. Results and Discussion

2.1. Time-Dependent Study of Ionothermal Crystallization of SAPO-11

In this work, SAPO-11 is crystallized under ionothermal conditions (150 °C) using 1-propylpyridinium bromide ([PPy]Br) as both structure-directing agent and solvent, which is different from the hydrothermal technique applied in the classical zeolite synthesis system. At 50 h, no solid product was recovered upon centrifugation, indicating the complete dissolution and participation of inorganic reactants in the ionic liquid. At 110 h, a small amount of amorphous nanoparticles (140 nm) was formed and sedimented, indicating that the polymerization of inorganic Si, Al and P oligomers into a heavier solid had taken place (E-1, Figure 1a) [27]. A semicrystalline SAPO-11 product, consisting of spherical amorphous nanoparticles (ca. 270 nm) and broomstick-like particles (ca. 1.9 μm), starts to form at 120 h revealing the occurrence of nucleation (E-2, Figure 1b).

The XRD amorphous hump completely disappears after 133 h of ionothermal heating, and the XRD pattern of the E-3 solid displays intense peaks which can perfectly match with the simulated XRD pattern of AEL-type zeolite (E-3, Figure 1c) [28]. Meanwhile, the Fe-SEM confirms that all the amorphous nanoparticles were consumed as nutrients for the growth of SAPO-11 (Figure 1c) [29]. As a result, large and well-defined broomstick crystals (ca. 2.3 μm) are formed, completely different from those crystallized in other systems (screw-like [9], nanoaggregate [30], and columnar [31]). However, after 200 h of heating, the XRD analysis shows cocrystallization of SAPO-11 with SAPO-5 (AFI topology) (2θ = 7.43°, 20.97° and 22.38°) as a minor phase in the E-4 sample [28], thus revealing the metastability of SAPO-11 zeolite.
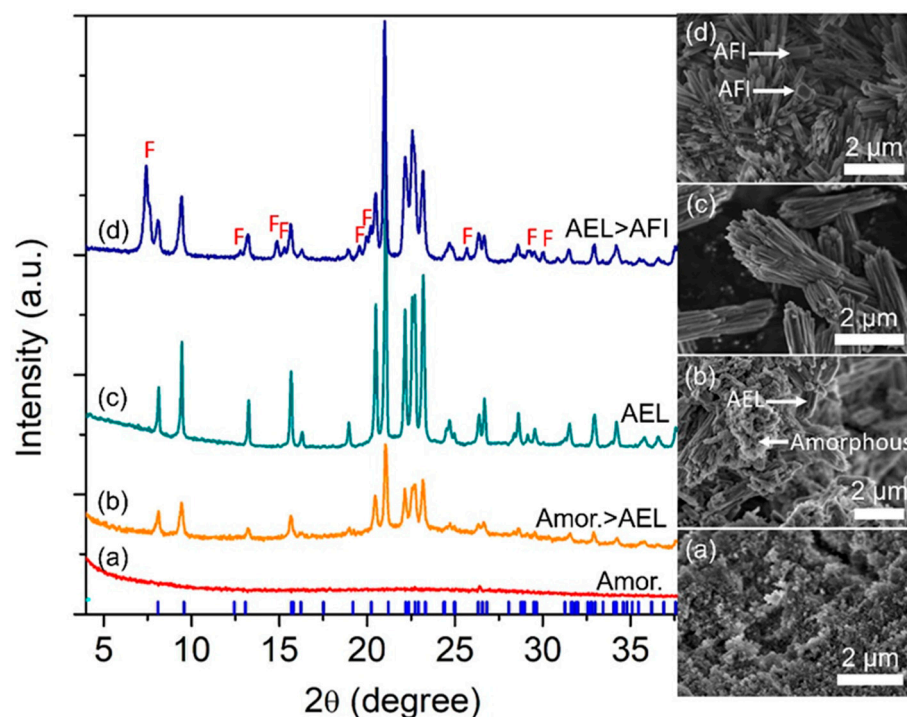
Figure 1. XRD patterns and FESEM images of (**a**) E-1, (**b**) E-2, (**c**) E-3 and (**d**) E-4 samples ionothermally heated at 150 °C for 110 h, 120 h, 133 h and 200 h, respectively. F denotes the presence of AFI crystalline phase. The theoretical XRD peak positions of the AEL phase are shown as vertical blue lines.

2.2. Effect of Synthesis Conditions

2.2.1. Effect of Heating Temperature

The heating temperature is very important for chemical processes as it provides energy to initiate the reactions [32]. Hence, the ionothermal synthesis of SAPO-11 was performed by heating the ionogel of 1.0Al: 1.8P: 0.3Si: 38[PPy]Br at 130 °C, 140 °C, 150 °C and 160 °C (denoted as E-5, E-6, E-3 and E-7, respectively) for 133 h to study its influence on the crystallization profile of SAPO-11. A low temperature seems to be insufficient to promote crystallization: the E-5 is produced as an amorphous nanospherical solid (ca. 20 nm) while E-6 contains rarely stick-like SAPO-11 crystals (ca. 940 nm) in the amorphous solids (Figure 2a,b). Only several XRD peaks due to SAPO-11 are shown ($2\theta = 9.36°$ [020], 20.41° [310], 21.11° [002], 22.23° [231], 22.68° [141] and 23.13° [240]). The XRD peaks are broadened, revealing small SAPO-11 crystallites, as also confirmed by the FE-SEM data [33]. By providing more energy through increasing the temperature to 150 °C, it is possible to see the full crystallization of SAPO-11 zeolite which results in the emergence of typical AEL X-ray diffraction peaks (E-3, Figure 2c). As shown, the SAPO-11 exhibits broomstick-like features, while the morphological structure strongly depends on the synthesis technique (e.g., hydrothermal, ionothermal, dry gel conversion, microwave heating, etc.), hydrophilicity and type of ionic liquid used [34]. Supplying excessive energy by raising the temperature to 160 °C leads to the activation and crystallization of a more stable crystalline phase, where a partial transformation of SAPO-11 into berlinite metasomatic phosphate (a nonporous crystalline dense phase) occurs (E-7, Figure 2d). Hence, 150 °C is the optimum temperature for crystallizing SAPO-11 in an ionothermal environment.
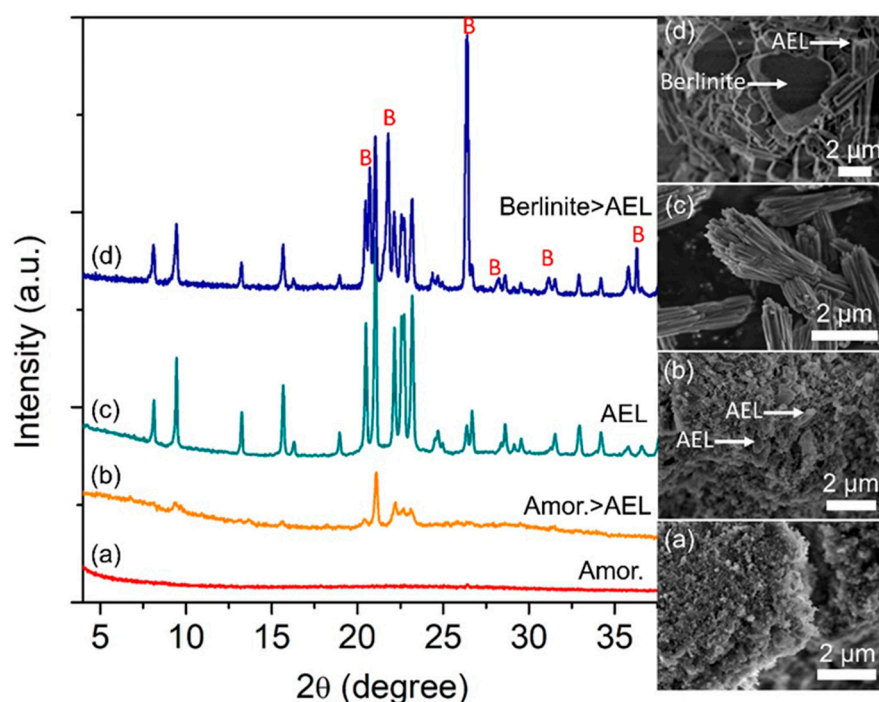
Figure 2. XRD patterns and FESEM micrographs of (**a**) E-5, (**b**) E-6, (**c**) E-3 and (**d**) E-7 samples prepared using the ionogel of 1.0Al: 1.8P: 0.3Si: 38[PPy]Br and heated at 130 °C, 140 °C, 150 °C and 160 °C for 133 h, respectively.

2.2.2. Effect of P/Al Molar Ratio

The amount of phosphorus added (in H_3PO_4 form) to the ionogel plays a very important role in the crystallization process, because phosphorus is one of the main components of SAPO-11 zeolite besides aluminum and silicon. In addition, H_3PO_4 also modulates the pH of the ionogel, which can alter the entire crystallization environment of zeolites [35]. Thus, the amount of H_3PO_4 (presented in P/Al molar ratio) is studied by heating the ionogel of 1.0Al: xP: 0.3Si: 38[PPy]Br (x = 1.2: E-8, x = 1.8: E-3, x = 2.1: E-9, x = 2.4: E-10) at 150 °C for 133 h. When x = 1.2, an amorphous solid with irregular shape, as proven by the broad XRD hump at 2θ = 20°–33°, is observed (Figure 3a). Increasing P content to x = 1.8, we witness the complete conversion of the amorphous solid into SAPO-11. This reveals the importance of H_3PO_4 in providing an adequate pH environment for the promotion of nucleation and crystal growth [36]. However, further increasing the x values to 2.1 and 2.4 produces a more acidic ionogel that favorably crystallizes berlinite dense phase and AFI-type zeolite, and this observation is in line with the work reported by Khoo et al. [37].

2.2.3. Effect of Si Content

As mentioned, the element Si is another primary building unit component of the SAPO-11 zeolite framework that controls the crystallization process [38]. In addition, the isomorphous substitution of Si^{4+} into the SAPO-11 framework may result in variable physiochemical attributes (e.g., creating acid sites) which are highly demanding in heterogeneous catalysis [39]. Hence, the amount of Si content in ionogels of 1.0Al: 1.8P: ySi: 38[PPy]Br was varied (y = 0, 0.4, 0.9 and 1.3) to study its effects on the crystallization kinetics of SAPO-11. When no Si (y = 0) is added, tridymite (2θ = 21.6° [112] and 21.8° [−404]) as a competing phase is formed together with SAPO-11 (E-11, Figure 4a). The results from the FE-SEM micrograph also agree with the XRD data showing that bulk SAPO-11 crystals with stick-like shape (14 μm) are cocrystallized with hexagonal tridymite crystals. When y = 0.4, both phases remain dominant, with a small amount of SAPO-5 (AFI topology) phase (2θ = 7.42° [100]) detected (E-12, Figure 4b). In SEM, the SAPO-5 zeolite

can be characterized by its hexagonal rod morphology, which is commonly reported for AFI-type molecular sieves [40]. SAPO-11 is formed at the expense of tridymite as the Si content increases until fully pure SAPO-11 is obtained at $y = 1.3$ (E-3, Figure 4d). Hence, the results show that varying the Si content has a considerable effect on phase selectivity during the ionothermal process [41].
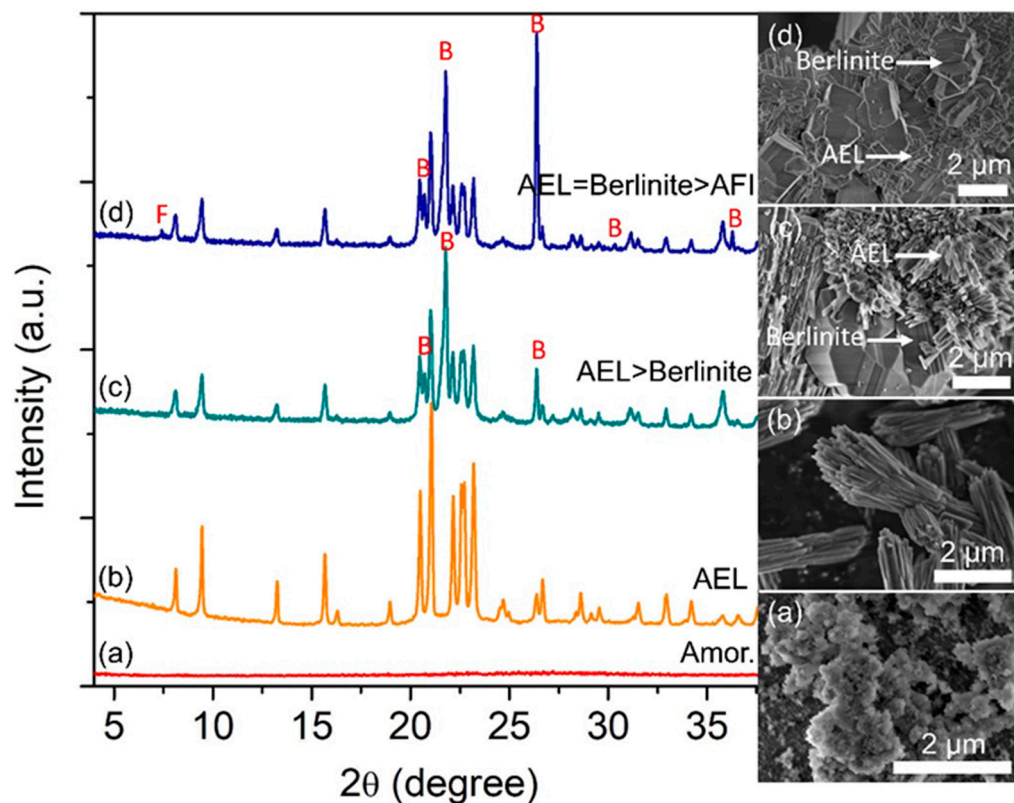

Figure 3. XRD patterns and FESEM images of (**a**) E-8 ($x = 1.2$), (**b**) E-3 ($x = 1.8$), (**c**) E-9 ($x = 2.1$) and (**d**) E-10 ($x = 2.4$) samples. The samples were prepared using the ionogel of 1.0Al: xP: 0.3Si: 38[PPy]Br heated at 150 °C for 133 h. F and B denote the presence of AFI and berlinite crystalline phases, respectively.

2.2.4. Effect of [PPy]Br Content

An ionic liquid is essential for controlling the concentration of raw chemicals besides serving as a solvent for the ionothermal synthesis of zeolite [42]. Simultaneously, it also acts as a potent structure-directing agent in the formation of zeolites. Hence, the precursor mixture of 1.0Al: 1.8P: 0.3Si: z[PPy]Br ($z = 14, 22, 30$ and 38) was heated at 150 °C for 133 h in order to investigate the effects of [PPy]Br on the crystal evolution of SAPO-11. When $z = 14$, the tridymite dense phase tends to be crystallized as the major crystalline product with SAPO-5 (AFI) and SAPO-11 (AEL) as minor phases (E-14, Figure 5a). According to Basina et al., an insufficient amount of ionic liquid may cause slow and inefficient dissolution of inorganic reactants, affecting the equilibrium concentration for initiating the nucleation of zeolite crystals [43]. If the [PPy]Br content is increased to $z = 22$ or 30, it allows better dissolution of reactants, resulting in the favored crystallization of SAPO-11 over tridymite (E-14, Figure 5b,c). The optimum [PPy]Br content is found to be $z = 38$, when pure SAPO-11 solid is obtained. Hence, besides serving as solvent, [PPy]Br also plays a structure-directing role and a charge-balancing role in stabilizing the micropore channel system of SAPO-11 [44].
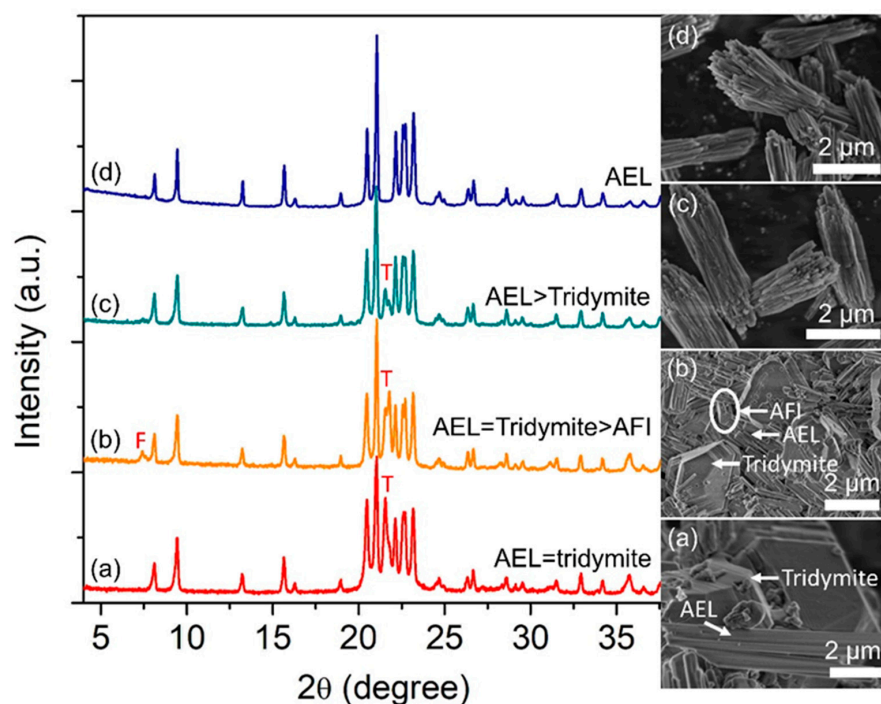
Figure 4. XRD patterns and FESEM micrographs of (**a**) E-11 ($y = 0$), (**b**) E-12 ($y = 0.4$), (**c**) E-3 ($y = 0.9$) and (**d**) E-13 ($y = 1.3$) samples. The samples were prepared using the ionogel of 1.0Al: 1.8P: ySi: 38[PPy]Br heated at 150 °C for 133 h. F and T denote the presence of AFI and tridymite crystalline phases, respectively.
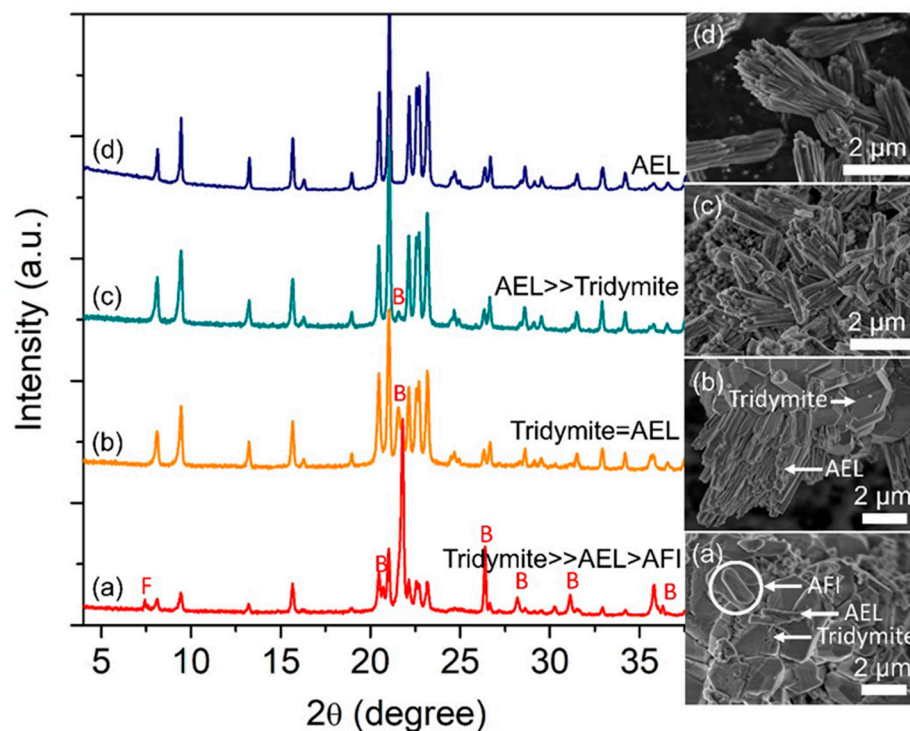

Figure 5. XRD patterns and FESEM micrographs of (**a**) E-14 ($z = 14$), (**b**) E-15 ($z = 22$), (**c**) E-16 ($z = 30$) and (**d**) E-3 ($z = 38$) samples. The samples were prepared using the ionogel of 1.0Al: 1.8P: 0.3Si: z[PPy]Br heated at 150 °C for 133 h. F and B denote the presence of AFI and berlinite crystalline phases, respectively.

2.3. Pore Stabilization and Confinement Roles of PPy]Br in SAPO-11

Thermogravimetry analysis can reveal the roles of [PPy]Br in stabilizing the AEL framework and the strength of this supramolecule's interaction with the SAPO-11 pore channel system.

In this regard, TGA/DTG data of pure [PPy]Br ionic salt and as-synthesized SAPO-11 (E-3) that contains occluded [PPy]Br were recorded. The free [PPy]Br exhibits one-step weight loss (96.5%) at 190–300 °C due to the decomposition of ionic liquid (Figure 6a) [45]. In contrast, the noncalcined SAPO-11 displays three steps of weight loss. The first weight-loss step (0.6%), at <170 °C, is due to the desorption of water from the surface of SAPO-11 [46], whereas the second (3.0%, 170–320 °C) and third (3.8%, 320–450 °C) steps of weight loss are attributed to the decomposition of the ionic liquid molecules [47]. As calculated, the $[PPy]^+/TO_2$ (T = Si, Al or P) molar ratio of as-synthesized SAPO-11 is 0.036, which corresponds to ca. 28 TO_2 primary building units enfolding one $[PPy]^+$ organic cation in a three-dimensional manner. In addition, the weight loss of organic moiety occurs at a higher temperature due to strong interaction and confinement effects of the [PPy]Br molecule in the micropores. As a result, the trapped [PPy]Br requires a longer time and higher temperature to escape from the SAPO-11 pore channels [18]. Hence, it is revealed that the encapsulation of $[PPy]^+$ follows the "ship in a bottle" approach, whereby TO_2 primary building units form oligomers and then polymers around the $[PPy]^+$ (4.33 Å × 7.93 Å × 2.54 Å) [48] before the organic cation is tightly wrapped and confined in the pores forming a pore size diameter of 4.63 Å.
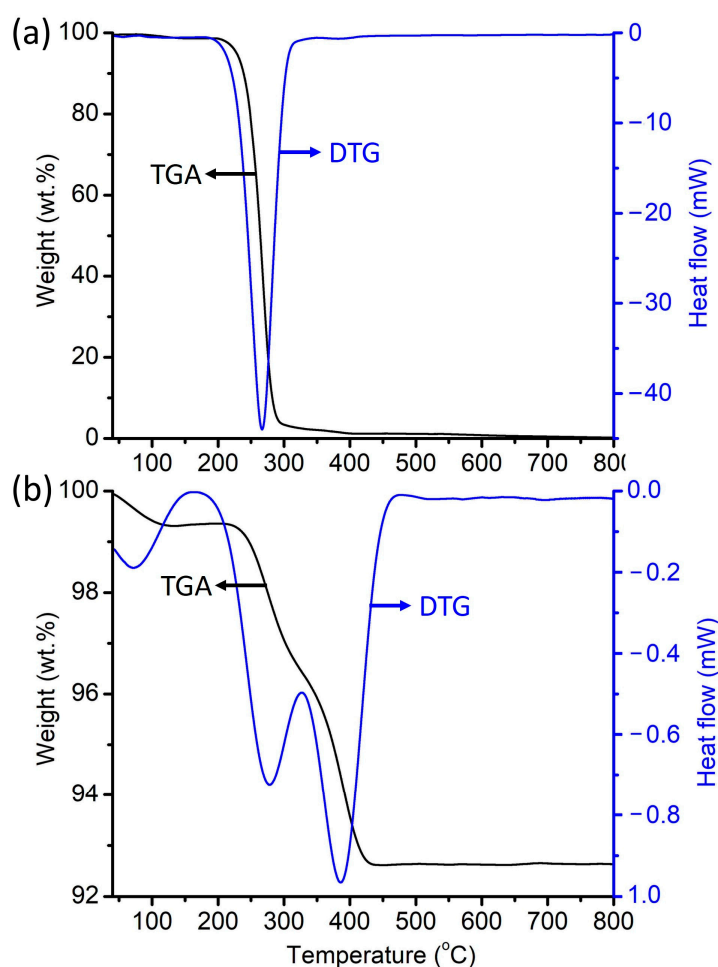

Figure 6. TGA/DTG curves of (**a**) free [PPy]Br ionic salt and (**b**) as–synthesized SAPO-11 (E-3).

The ^{13}C NMR spectroscopy also shows that the [PPy]Br is intact after being trapped inside the SAPO-11 micropores; all NMR peaks due to [PPy]Br molecules are shown in the as-synthesized SAPO-11 (Figure 7b). In this sample, the ionic liquid molecules (especially C1, C3 and C6) also experience chemical shifts compared with their free counterpart (Figure 7a). Furthermore, their resonance bands are also broadened, indicating strong molecule-wall interaction and geometric constraints in confined space that disallow molecular movement inside SAPO-11 micropores [49]. Thus, the thermogravimetry and NMR data further confirm the stabilizing and pore-filling effect roles of [PPy]Br during the crystallization of SAPO-11.
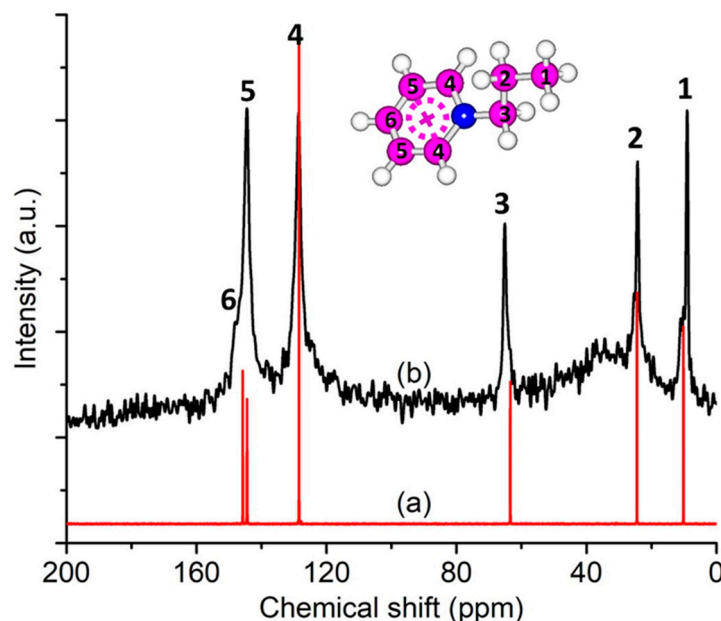

Figure 7. (a) Liquid state NMR spectrum of [PPy]Br ionic molten salt, and (b) solid state MAS NMR spectrum of as-synthesized SAPO-11 (E-3).

2.4. Porous and Acid Properties of [PPy]Br Synthesized SAPO-11

The purity, crystallinity and catalytic performance of SAPO-11 are directly related to its porous properties, and hence, nitrogen adsorption–desorption analysis was performed on the calcined SAPO-11 at −196 °C. The N$_2$ adsorption–desorption curves of SAPO-11 display type I adsorption isotherm due to its high microporous characteristics (S_{Mic} = 110 m^2 g^{-1}) with some N$_2$ uptake at high P/P$_o$, confirming its secondary textural mesoporosity (Table 1, Figure 8 and inset) [50]. The sample also shows a considerably high surface area (S_{BET} = 149 m^2 g^{-1}, S_{Mic} = 110 m^2 g^{-1}), high total pore volume (V_{tot} = 0.24 cm^3 g^{-1}) and large average pore diameter (d_p = 29.5 nm where primary micropores and secondary textural mesopores are considered), whereby its porosity is comparable with the SAPO-11 synthesized using dipropylamine under hydrothermal conditions (S_{BET} = 100 m^2 g^{-1}, S_{Mic} = 50 m^2 g^{-1}, V_{tot} = 0.15 cm^3 g^{-1} [51]).

Table 1. Surface acidity of SAPO-11 calculated using pyridine-IR spectroscopy method. B = Brønsted acid sites and L = Lewis acid sites.

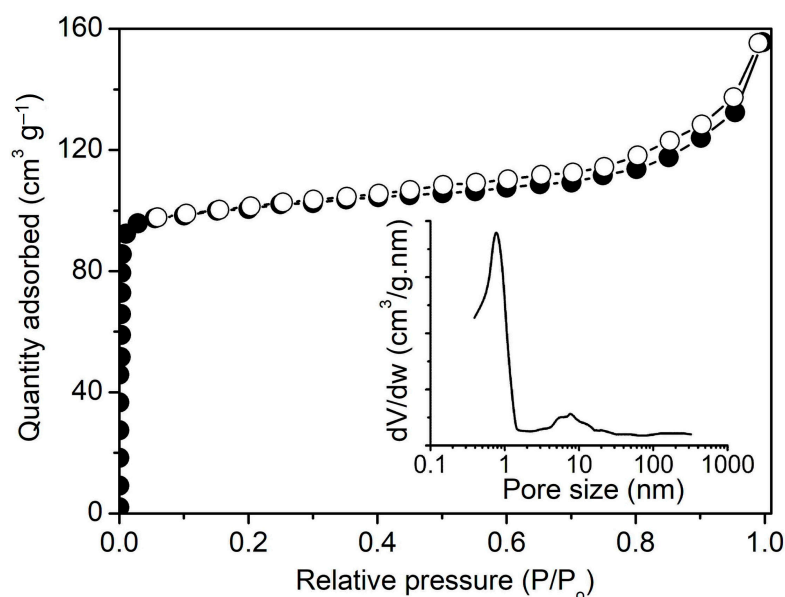| Sample	Total Acidity (150 °C) (μmol g^{-1})			Medium-to-Strong Acidity (300 °C) (μmol g^{-1})		
	B	**L**	**B+L**	**B**	**L**	**B+L**
SAPO-11	136	158	294	61	40	101

Figure 8. Nitrogen adsorption (close symbols) and desorption (open symbols) isotherms and (inset) pore size distribution of calcined SAPO-11 (E-3) sample at −196 °C.

FTIR spectroscopy investigation of pyridine adsorption is one of the most popular methods for characterizing the surface acidity. The study of the framework acidity (type, amount and strength) is based on the bonding strength of the N nucleophile group of pyridine to the acid sites of SAPO-11 (Si species) [52]. The FTIR spectra of pyridine adsorbed SAPO-11 after desorption at 150 and 300 °C are shown (Figure 9). In general, the SAPO-11 contains both Lewis and Brønsted acidities, based on the IR bands at 1455 and 1545 cm^{-1}, respectively. The Lewis acid sites (158 μmol g^{-1}), which come from structural defects after calcination, are higher than the Brønsted acid sites (136 μmol g^{-1}) (Table 2, Figure 9) [53]. The quantity of acidity of SAPO-11 at 300 °C is also determined where it can distinguish the strength of acid sites. It can be seen that some IR bands are still retained, indicating the presence of medium-to-strong Lewis (40 μmol g^{-1}) and Brønsted (61 μmol g^{-1}) acid sites in the solid. Hence, the results show that the synthesized SAPO-11 is a mild-to-strong acid solid catalyst with a total acidity slightly higher than that of the conventional SAPO-11 [54].
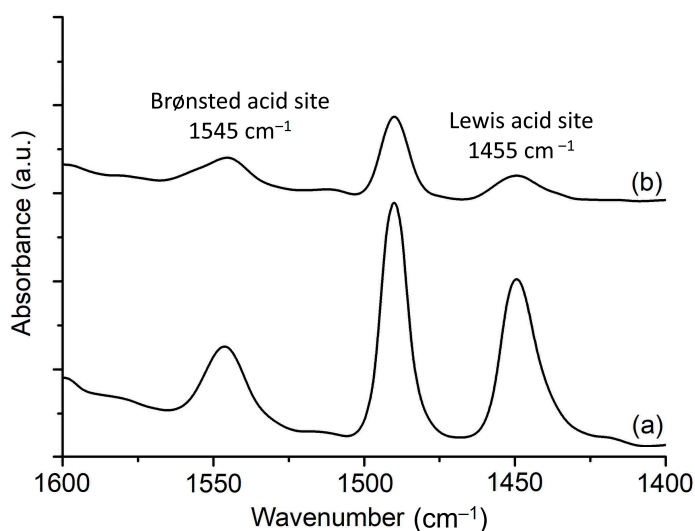

Figure 9. IR spectra of pyridine adsorption after desorption at (a) 150 °C and (b) 300 °C.

Table 2. The chemical composition of ionogel, crystallization time, heating temperature and phase products obtained for the synthesis parameters effect study.

Sample	Variable Parameter	Ionogel Molar Composition				T (°C)	t (h)	Products *
		Al	P	Si	[PPy]Br			
E-1	Crystallization time, t	1.0	1.8	0.3	38	150	110	Amorphous
E-2							120	Amorphous > AEL
E-3							133	AEL
E-4							200	AEL > AFI
E-5	Heating temperature, T	1.0	1.8	0.3	38	130	133	Amorphous
E-6						140		Amorphous > AEL
E-3						150		AEL
E-7						160		Berlinite > AEL
E-8	P	1.0	1.2	0.3	38	150	133	Amorphous
E-3			1.8					AEL
E-9			2.1					AEL > Berlinite
E-10			2.4					AEL = Berlinite > AFI
E-11	Si	1.0	1.8	0	38	150	133	AEL = Berlinite
E-12				0.1				AEL = Tridymite > AFI
E-3				0.2				AEL > Tridymite
E-13				0.3				AEL
E-14	[PPy]Br	1.0	1.8	0.3	14	150	133	Tridymite >> AEL > AFI
E-15					22			Tridymite = AEL
E-16					30			AEL >> Tridymite
E-3					38			AEL

* AEL = SAPO-11, AFI = SAPO-5.

2.5. Catalytic Study

Conversion of levulinic acid into ethyl levulinate via esterification was used as a probe reaction (Scheme 1) to study the catalytic behavior of SAPO-11 under conductive instant heating conditions. Before use, the calcined SAPO-11 was checked with TGA/DTG to ensure that all ionic liquid had been removed. Without adding any catalyst, the rate of levulinic acid conversion is very low (6.6%) after 60 min of heating at 150 °C. This indicates that the esterification of levulinic acid is an activated reaction. Interestingly, the conversion is enhanced tremendously when SAPO-11 is added, after which 75.5% of conversion is recorded after heating at 150 °C for 20 min, revealing that SAPO-11 is a potential active catalyst for the conversion of levulinic acid into ethyl levulinate (Figure 10A(a)).
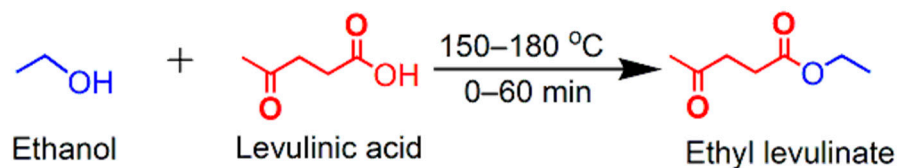
Scheme 1. Esterification of levulinic acid and ethanol for producing ethyl levulinate.
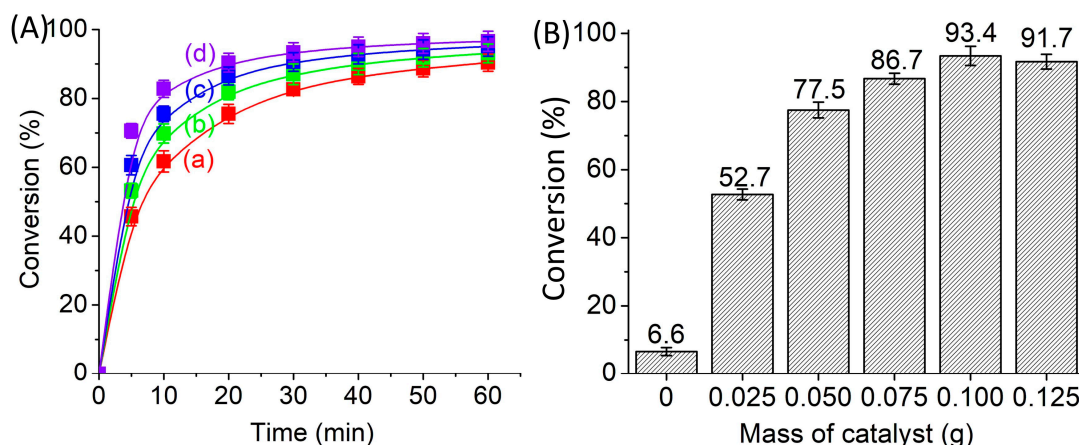
Figure 10. (**A**) Conversion of levulinic acid via esterification enhanced by SAPO-11 (E-3) catalyst at (a) 150 °C, (b) 160 °C, (c) 170 °C and (d) 180 °C under conductive instant heating using reaction conditions: $m_{SAPO-11}$ = 0.100 g, levulinic acid:ethanol ratio = 1:11, and (**B**) effect of catalyst loading on the conversion of levulinic acid using reaction conditions: temperature = 180 °C, time = 30 min, levulinic acid:ethanol ratio = 1:11.

The esterification reaction was also investigated at various temperatures (150–180 °C) from 0 to 60 min. The reaction conversion is enhanced by increasing the heating temperature, as shown in Figure 10A. This is due to the fact that when more energy is provided to the system, the reaction rate increases, as stated by the Arrhenius equation [55]. For instance, at 30 min of reaction, 82.6% of conversion is recorded at 150 °C, and this increases to 87.0% (160 °C) and 90.6% (170 °C) before reaching 93.4% at 180 °C (Figure 10A(a–d)). Based on the reaction study, the optimum reaction time and temperature are 30 min of heating at 180 °C, because the conversion rate nearly plateaus after 30 min.

The effect of catalyst amount was also studied at 180 °C for 30 min with a molar ratio of 1:11 (levulinic acid:ethanol) using 0–0.125 g of SAPO-11. Without catalyst, the conversion rate is merely 6.6%, and the levulinic acid conversion rate rises significantly to 52.7% when 0.025 g catalyst is added (Figure 10B). The conversion rate keeps increasing to 93.4% with the catalyst load increased to 0.100 g. Such a phenomenon can be explained by the high availability of Brønsted acid sites when more solid acid catalyst is added, resulting in a high reaction conversion. However, the levulinic acid conversion slightly decreases when the catalyst loading is further increased to 0.125 g (91.7%), which may be due to the excessive catalyst loading causing inefficient stirring [56]. Furthermore, the water molecules produced during the esterification reaction can also deactivate the SAPO-11 catalyst's active sites, and this compromises the effectiveness of the catalyst [57]. Therefore, 0.100 g of SAPO-11 catalyst is the ideal loading.

The catalytic performance of SAPO-11 is also compared with conventional homogeneous catalysts (H_2SO_4, HCl, acetic acid, *p*-toluenesulfonic acid) at 180 °C for 30 min of instant heating (Figure 11a). It is shown that both H_2SO_4 and HCl achieve 100% conversion, but their selectivity towards ethyl levulinate are merely 86.3% and 90.1%, respectively; 4-ethoxy γ-valerolactone and alpha-Angelica lactone were produced as by-products in both catalyzed reactions. For acetic acid, a low conversion rate (74.2%) with 100% selectivity of ethyl levulinate are recorded; this can be explained by its weak acidity. On the other hand, SAPO-11 shows comparable catalytic performance to that of *p*-toluenesulfonic acid, achieving nearly 95% conversion and excellent 100% ethyl levulinate selectivity. The superior performance of SAPO-11 can hence be explained by its mild-to-strong acidity and unidimensional 10-membered ring pore channel (4.63 × 2.01 × 2.01 Å^3) that exhibits good molecular size-sieving ability for selectively producing only ethyl levulinate as a single product.

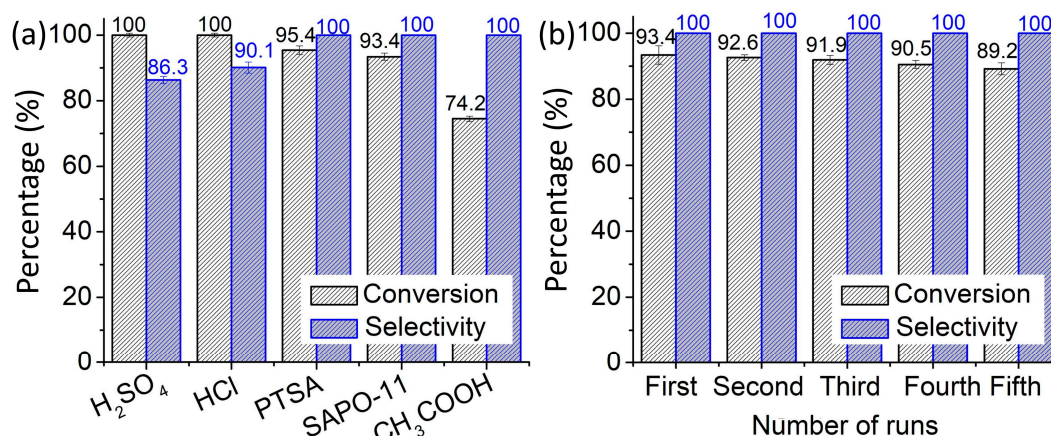**Figure 11.** (**a**) Comparison of catalytic activity between synthesized SAPO-11 and conventional homogeneous acids and (**b**) SAPO-11 catalyst reusability test. Reaction conditions: T = 180 °C, t = 30 min, levulinic acid:ethanol ratio = 1:11, $m_{SAPO-11}$ = 0.100 g (17.98 μmol) equivalent to 0.0017 g of HCl, 0.0018 g of H_2SO_4, 0.0011 g of CH_3COOH and 0.0035 g of *p*-toluenesulfonic acid (PTSA).

Although some homogeneous catalysts achieve 100% conversion, they are not reusable. On the other hand, the SAPO-11 catalyst is recyclable, and the reaction performance is nearly maintained even after five consecutive cycles of reaction (Figure 11b). Thus, being reusable, ecofriendly and not corrosive, SAPO-11 is preferable to its homogeneous counterparts as an acid catalyst in the esterification of levulinic acid into ethyl levulinate. Comprehensive works on synthesizing various zeolite materials using other pyridinium ionic liquids for advanced applications (e.g., membrane, catalyst) are in progress.

3. Methodology

3.1. Synthesis of 1-Propylpyridinium Bromide, [PPy]Br

Scheme 2 illustrates the synthesis procedure of a novel [PPy]Br ionic liquid. Typically, pyridine (94.846 g, 99%, Acros Organics, Geel, Belgium) and 1-bromopropane (221.20 g, 99%, Acros Organics, Geel, Belgium) were mixed together in a 500-mL round bottom flask. Then, the mixture was magnetically stirred and refluxed at 70 °C for 20 h. The mixture was subjected to rotary evaporation (100 rpm) at 60 °C under a vacuum (50 mbar) to remove the nonreacted 1-bromopropane. The obtained yellowish solid was then soaked (4 h) and washed with acetone (200 mL) 4 times before it was dried in an oven at 105 °C overnight to obtain the 1-propylpyridinium bromide ([PPy]Br) ionic salt. Yield: 86.2%. ^{1}H NMR (500 MHz, D_2O): δ = 1.01 (3H, t, *J* = 7.2 Hz, pyridine N-CH_2-CH_2-C*H$_3$*), 2.11 (2H, m, *J* = 7.25, pyridine N-CH_2-C*H$_2$*-CH_3), 4.71 (2H, t, *J* = 7.23 Hz, pyridine N-C*H$_2$*), 8.17 (2H, t, *J* = 6.3 Hz, pyridine N-CH=C*H*), 8.64 (1H, t, *J* = 7.77 Hz, pyridine N-CH=CH-C*H*), 8.96 (2H, d, *J* = 5.7 Hz, pyridine N=C*H*). ^{13}C NMR (500 MHz, D_2O): δ = 10.26, 24.05, 63.71, 127.84, 144.01, 145.55. FTIR (KBr disk) cm^{-1}: 1167 (C–N), 1486 (C=N), 1501 and 1634 (aromatic C=C), 2879 (C_{sp}^3–H), 3055 (C_{sp}^2–H), 3407 cm^{-1} (broad, O–H). Anal. Cacld. for $C_8H_{12}NBr$: C, 47.54%; H, 5.95%; N, 6.92%; found: C, 46.83%; H, 5.85%; N, 6.86%.
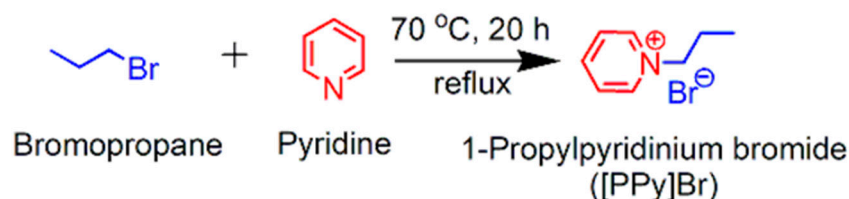
Scheme 2. The synthesis route of 1-propylpyridinium bromide ([PPy]Br) ionic liquid.

3.2. Ionothermal Synthesis of Silicoaluminophosphate Number 11 (SAPO-11)

Initially, aluminum isopropoxide (0.192 g, 98%, Sigma-Aldrich, Darmstadt, Germany) was placed into a Teflon-lined stainless-steel autoclave. Next, the [PPy]Br ionic liquid (7.000 g), phosphoric acid (0.192 g, 85%, Sigma-Aldrich, Darmstadt, Germany) and tetraethyl orthosilicate (0.056 g, 98%, Sigma Aldrich, Darmstadt, Germany) were subsequently added. The final chemical composition had a molar ratio of 1.0Al: 1.8P: 0.3Si: 38[PPy]Br. The autoclave was capped and placed in an oven at 150 °C for various crystallization times (110–200 h). The mixture was dispersed in distilled water and the sedimented solid product was recovered using high-speed centrifugation (10,000 rpm, 5 min, Drawell, Chongqing, China). The process of dispersion and purification with distilled water was repeated another three times before the final solid product was dried at 90 °C overnight. The resulting as-synthesized SAPO-11 was calcined at 580 °C for 6 h at a ramping rate of 1 °C min^{-1} under air atmosphere.

For the study of the effects of synthesis variables (heating temperature, phosphorous content, silicon amount and [PPy]Br concentration), a similar synthesis procedure was applied wherein the resulting ionogel with a chemical composition of 1.0Al: xP: ySi: z[PPy]Br (x = 1.2–2.4, y = 0–0.3, z = 30–54) was heated at 130–160 °C for 133 h. The crystallization conditions of the solids are summarized in Table 2.

3.3. Characterization

The functional groups of the ionic liquid were confirmed using a Perkin Elmer's System 2000 infrared spectrometer (resolution 4 cm^{-1}, 100 scans, Waltham, MA, USA) where the KBr pellet technique was applied (KBr:sample mass ratio = 60:1). The liquid's 1H and 13C NMR spectra were recorded with a Bruker Advance 500 MHz spectrometer (Waltham, MA, USA) operated at 500 and 126 MHz for ^{1}H and ^{13}C, respectively, using a single pulse excitation with $\pi/2$ (3 µs) pulses. In both analyses, deuterium oxide (D_2O) and tetramethylsilane (TMS) were used as the solvent and internal standard for chemical shift, respectively. The elemental constituents of the [PPy]Br ionic liquid were determined using a Perkin Elmer 2400 Series II CHNS/O analyzer (Waltham, MA, USA). The crystallization process and crystalline phase of solid samples were studied using a Bruker D8 AVANCE diffractometer (Waltham, MA, USA) operated at a scanning rate of 0.2° min^{-1} and 40 kV/10 mA with the copper Kα radiation source (λ = 1.5406 Å). The crystal size and morphology of solids were analyzed using a HITACHI Regulus 8220 FE-SEM (Tokyo, Japan) at low acceleration voltage (2 kV). The porous properties of SAPO-11 were studied using a Micromeritics ASAP 2010 analyzer (Norcross, GA, USA) where the sample (ca. 80 mg) was first degassed at 250 °C for 10 h and then subjected to N_2 adsorption-desorption at −196 °C. The specific surface area, micropore surface area and pore size distribution were determined using the Brunauer–Emmett–Teller (BET), t-plot and non-localized density functional theory (NLDFT) models, respectively, while the total pore volume was calculated using the total N_2 uptake at P/P_o = 0.998. The surface acidity of the synthesized SAPO-11 was investigated with the in situ pyridine-FTIR spectroscopy technique. First, a self-supporting wafer of sample (ca. 12 mg) was degassed at 300 °C for 4 h under vacuum (10^{-3} mbar). After cooling down to room temperature, the reference spectrum was collected (8 cm^{-1} resolution, 200 scans). Pyridine was adsorbed onto the sample for 3 min prior to the evacuation of non-adsorbed pyridine and heating at 150 °C for 1 h to remove physisorbed pyridine. The spectrum was recorded after cooling. The wafer was heated again at 300 °C for 1 h before an IR spectrum was collected. The number of Brønsted and Lewis acid sites was calculated using molar integral extinction coefficients of $\varepsilon_{Brønsted}$ = 0.73 cm µmol^{-1} and ε_{Lewis} = 0.96 cm µmol^{-1} [58].

3.4. Catalytic Reaction Study

The esterification of levulinic acid and ethanol into ethyl levulinate over an E-3 sample (hereafter referred to as SAPO-11) was performed under conductive instant heating conditions that mimic rapid microwave heating. Initially, the calcined SAPO-11

(0.100 g) was activated at 300 °C for 3 h before it was mixed with levulinic acid (0.04 g, 0.34 mmol, 98%, Acros Organic) and ethanol (0.202 g, 4.38 mmol, 99.7%, Qrec) in a 10-mL glass vial. The mixture was capped and heated in an Anton Paar's Monowave 50 conductive instant heating reactor (Graz, Austria) at 150–180 °C for 0–60 min under magnetic stirring (800 rpm). The catalyst was separated using centrifugation (10,000 rpm, 10 min, Drawell, Chongqing, China) and the reaction liquid (1 μL) was withdrawn and injected into a GC-MS (Agilent 7000 Series Triple Quad, Santa Clara, CA, USA) and a GC-FID (Agilent's HP6890 GC, Santa Clara, CA, USA) for qualitative and quantitative analyses, respectively; toluene (98%, Merck) was used as an internal standard. Each experiment was repeated twice, and error bars were plotted based on the two replicate experiments.

4. Conclusion

In conclusion, SAPO-11 has successfully been crystallized under ionothermal conditions using a novel 1-propylpyridinium bromide ([PPy]Br) ionic liquid as both solvent and structure-directing agent. By carefully inspecting the crystallization process, pure SAPO-11 can be crystallized at 150 °C after 133 h of ionothermal heating. In addition, the effects of synthesis parameters (viz. crystallization temperature, phosphorous content, silicon amount and [PPy]Br concentration) were investigated and we showed that moderate temperature, low P amount, and high Si and [PPy]Br contents are essential for minimizing the cocrystallization of other crystalline phases (e.g., AFI, berlinite and tridymite). The synthesized SAPO-11 has a high surface area (149 m^2 g^{-1}) and exhibits Brønsted and Lewis acidities which are beneficial for the esterification of levulinic acid and ethanol. Under conductive instant heating conditions, the SAPO-11 catalyst gives excellent performance; 93.4% conversion and 100% selectivity of ethyl levulinate are achieved within 30 min at 180 °C, and this result is comparable to or even better than those of conventional homogeneous catalysts. From the viewpoint of materials chemistry, the use of a new class of pyridinium ionic liquids in ionothermal synthesis opens up enormous possibilities for crystallizing various zeolite molecular sieves with unique characteristics suitable for engineering high-performance materials in catalysis and separation.

Author Contributions: Investigation and writing—original draft preparation, A.I.J.M.M. Mohammad; investigation, V.S.; resources, Z.M.E.-B.; data curation, L.M.; writing—review and editing and data curation, T.C.L., writing—review and editing, supervision, project administration, funding acquisition and conceptualization, E.-P.N. All authors have read and agreed to the published version of the manuscript.

Conflicts of Interest: The authors declare no conflict of interest.

References

1. Ng, E.-P.; Itani, L.; Sekhon, S.S.; Mintova, S. Selective capture of water using microporous adsorbents to increase the lifetime of lubricants. *ChemSusChem* **2009**, *2*, 255–260. [CrossRef] [PubMed]
2. Makertihartha, I.; Kencana, K.S.; Dwiputra, T.R.; Khoiruddin, K.; Mukti, R.R.; Wenten, I. Silica supported SAPO-34 membranes for CO_2/N_2 separation. *Microporous Mesoporous Mater.* **2020**, *298*, 110068. [CrossRef]
3. Dai, X.; Cheng, Y.; Wei, Q.; Si, M.; Zhou, Y. Small-crystal and hierarchical SAPO-11 molecular sieve synthesized via three-stage crystallization method and hydroisomerization performance of corresponding NiWS supported catalyst. *Fuel* **2022**, *324*, 124610. [CrossRef]
4. Blasco, T.; Chica, A.; Corma, A.; Murphy, W.; Agúndez-Rodríguez, J.; Perez-Pariente, J. Changing the Si distribution in SAPO-11 by synthesis with surfactants improves the hydroisomerization/dewaxing properties. *J. Catal.* **2006**, *242*, 153–161. [CrossRef]
5. Rabaev, M.; Landau, M.V.; Vidruk-Nehemya, R.; Koukouliev, V.; Zarchin, R.; Herskowitz, M. Conversion of vegetable oils on Pt/Al_2O_3/SAPO-11 to diesel and jet fuels containing aromatics. *Fuel* **2015**, *161*, 287–294. [CrossRef]

6.   Xing, G.; Liu, S.; Guan, Q.; Li, W. Investigation on hydroisomerization and hydrocracking of C15–C18 n-alkanes utilizing a hollow tubular Ni-Mo/SAPO-11 catalyst with high selectivity of jet fuel. *Catal. Today* **2019**, *330*, 109–116. [CrossRef]

7.   Xiao, Z.; Zhan, W.; Guo, Y.; Guo, Y.; Gong, X.; Lu, G. The synthesis of Co-doped SAPO-5 molecular sieve and its performance in the oxidation of cyclohexane with molecular oxygen. *Chin. J. Catal.* **2016**, *37*, 273–280. [CrossRef]

8.   Said, S.; Zaky, M.T. PtSn supported on hierarchical mesoporous SAPO-11: Synthesis, characterization and catalytic evaluation in n-heptane hydroisomerization. *J. Organomet. Chem.* **2021**, *957*, 122180. [CrossRef]

9.   Tiuliukova, I.; Rudina, N.; Lysikov, A.; Cherepanova, S.; Parkhomchuk, E. Screw-like morphology of silicoaluminophosphate-11 (SAPO-11) crystallized in ethanol medium. *Mater. Lett.* **2018**, *228*, 61–64. [CrossRef]

10. Auwal, I.A.; Mintova, S.; Ling, T.C.; Khoerunnisa, F.; Wong, K.-L.; Ng, E.-P. Crystallization profile and morphological study of SAPO-5 templated by imidazolium cations of different functional groups. *Microporous Mesoporous Mater.* **2020**, *308*, 110514. [CrossRef]

11. Ahmad, N.H.; Daou, T.J.; Maireles-Torres, P.; Zaarour, M.; Mintova, S.; Ling, T.-C.; Ng, E.-P. Morphological effects on catalytic performance of LTL zeolites in acylation of 2-methylfuran enhanced by non-microwave instant heating. *Mater. Chem. Phys.* **2020**, *244*, 122688. [CrossRef]

12. Parnham, E.R.; Morris, R.E. Ionothermal Synthesis of Zeolites, Metal–Organic Frameworks, and Inorganic–Organic Hybrids. *Accounts Chem. Res.* **2007**, *40*, 1005–1013. [CrossRef] [PubMed]

13. Wu, Q.; Hong, X.; Zhu, L.; Meng, X.; Han, S.; Zhang, J.; Liu, X.; Jin, C.; Xiao, F.-S. Generalized ionothermal synthesis of silica-based zeolites. *Microporous Mesoporous Mater.* **2019**, *286*, 163–168. [CrossRef]

14. Ng, E.-P.; Ghoy, J.-P.; Awala, H.; Vicente, A.; Adnan, R.; Ling, T.C.; Mintova, S. Ionothermal synthesis of FeAPO-5 in the presence of phosphorous acid. *Crystengcomm* **2015**, *18*, 257–265. [CrossRef]

15. Cooper, E.R.; Andrews, C.D.; Wheatley, P.S.; Webb, P.B.; Wormald, P.; Morris, R.E. Ionic liquids and eutectic mixtures as solvent and template in synthesis of zeolite analogues. *Nature* **2004**, *430*, 1012–1016. [CrossRef] [PubMed]

16. Welton, T. Room-Temperature Ionic Liquids. Solvents for Synthesis and Catalysis. *Chem. Rev.* **1999**, *99*, 2071–2084. [CrossRef]

17. Khoo, D.Y.; Awala, H.; Mintova, S.; Ng, E.-P. Synthesis of AlPO-5 with diol-substituted imidazolium-based organic template. *Microporous Mesoporous Mater.* **2014**, *194*, 200–207. [CrossRef]

18. Ng, E.-P.; Sekhon, S.S.; Mintova, S. Discrete MnAlPO-5 nanocrystals synthesized by an ionothermal approach. *Chem. Commun.* **2009**, *13*, 1661–1663. [CrossRef]

19. Fortas, W.; Djelad, A.; Hasnaoui, M.A.; Sassi, M.; Bengueddach, A. Adsorption of gentian violet dyes in aqueous solution on microporous AlPOs molecular sieves synthesized by ionothermal method. *Mater. Res. Express* **2018**, *5*, 025018. [CrossRef]

20. Lin, Y.; Wei, Y.; Zhang, L.; Guo, K.; Wang, M.; Huang, P.; Meng, X.; Zhang, R. Facile ionothermal synthesis of SAPO-LTA zeotypes with high structural stability and their catalytic performance in MTO reaction. *Microporous Mesoporous Mater.* **2019**, *288*, 109611. [CrossRef]

21. Ma, H.; Xu, R.; You, W.; Wen, G.; Wang, S.; Xu, Y.; Wang, B.; Wang, L.; Wei, Y.; Xu, Y.; et al. Ionothermal synthesis of gallophosphate molecular sieves in 1-alkyl-3-methyl imidazolium bromide ionic liquids. *Microporous Mesoporous Mater.* **2009**, *120*, 278–284. [CrossRef]

22. Xu, Y.-P.; Tian, Z.-J.; Wang, S.-J.; Hu, Y.; Wang, L.; Wang, B.-C.; Ma, Y.-C.; Hou, L.; Yu, J.-Y.; Lin, L.-W. Microwave-Enhanced Ionothermal Synthesis of Aluminophosphate Molecular Sieves. *Angew. Chem. Int. Ed.* **2006**, *45*, 3965–3970. [CrossRef] [PubMed]

23. Kore, R.; Srivastava, R. Synthesis of zeolite Beta, MFI, and MTW using imidazole, piperidine, and pyridine based quaternary ammonium salts as structure directing agents. *RSC Adv.* **2012**, *2*, 10072–10084. [CrossRef]

24. Dumitriu, E.; Azzouz, A.; Hulea, V.; Lutic, D.; Kessler, H. Synthesis, characterization and catalytic activity of SAPO-34 obtained with piperidine as templating agent. *Microporous Mater.* **1997**, *10*, 1–12. [CrossRef]

25. Prakash, A.M.; Unnikrishnan, S. Synthesis of SAPO-34: High silicon incorporation in the presence of morpholine as template. *J. Chem. Soc. Faraday Trans.* **1994**, *90*, 2291–2296. [CrossRef]

26. Shimizu, Y.; Ohte, Y.; Yamamura, Y.; Tsuzuki, S.; Saito, K. Comparative Study of Imidazolium- and Pyrrolidinium-Based Ionic Liquids: Thermodynamic Properties. *J. Phys. Chem. B* **2012**, *116*, 5406–5413. [CrossRef]

27. Wong, S.-F.; Deekomwong, K.; Wittayakun, J.; Ling, T.C.; Muraza, O.; Adam, F.; Ng, E.-P. Crystal growth study of K-F nanozeolite and its catalytic behavior in Aldol condensation of benzaldehyde and heptanal enhanced by microwave heating. *Mater. Chem. Phys.* **2017**, *196*, 295–301. [CrossRef]

28. IZA-SC Database of Zeolite Structures. Available online: http://www.iza-structure.org/databases/ (accessed on 12 January 2023).

29. Wong, J.-T.; Ng, E.-P.; Adam, F. Microscopic investigation of nanocrystalline zeolite L synthesized from rice husk ash. *J. Am. Ceram. Soc.* **2012**, *95*, 805–808. [CrossRef]

30. Chen, Z.; Dong, Y.; Jiang, S.; Song, W.; Lai, W.; Yi, X.; Fang, W. Low-temperature synthesis of hierarchical architectures of SAPO-11 zeolite as a good hydroisomerization support. *J. Mater. Sci.* **2017**, *52*, 4460–4471. [CrossRef]

31. Xu, X.T.; Zhai, J.P.; Li, I.L.; Ruan, S.C. Morphology Control of SAPO-11 and SAPO-47 Crystals in the Presence of Diethylamine. *Appl. Mech. Mater.* **2013**, *275–277*, 1737–1741. [CrossRef]

32. Choo, M.-Y.; Juan, J.C.; Oi, L.E.; Ling, T.C.; Ng, E.-P.; Noorsaadah, A.R.; Centi, G.; Lee, K.T. The role of nanosized zeolite Y in the H$_2$-free catalytic deoxygenation of triolein. *Catal. Sci. Technol.* **2019**, *9*, 772–782. [CrossRef]

33. Wong, S.-F.; Awala, H.; Vincente, A.; Retoux, R.; Ling, T.C.; Mintova, S.; Mukti, R.R.; Ng, E.-P. K-F zeolite nanocrystals synthesized from organic-template-free precursor mixture. *Microporous Mesoporous Mater.* **2017**, *249*, 105–110. [CrossRef]

34. Chen, D.; Tang, Q.; Deng, W.; Chaianansutcharit, S.; Guo, L. Comparative studies on the toluene sorption performance over silicalite-1 zeolites with different morphologies. *Microporous Mesoporous Mater.* **2022**, *346*, 112275. [CrossRef]

35. Wang, G.; Valldor, M.; Spielberg, E.T.; Mudring, A.-V. Ionothermal Synthesis, Crystal Structure, and Magnetic Study of Co_2PO_4OH Isostructural with Caminite. *Inorg. Chem.* **2014**, *53*, 3072–3077. [CrossRef] [PubMed]

36. Han, L.; Yan, X.; Guo, L.; Duan, Y.; Wang, Z.; Lu, T.; Xu, J.; Zhan, Y.; Wang, J. Ionothermal Synthesis of Triclinic SAPO-34 Zeolites. *Catalysts* **2021**, *11*, 616. [CrossRef]

37. Khoo, D.Y.; Kok, W.-M.; Mukti, R.R.; Mintova, S.; Ng, E.-P. Ionothermal approach for synthesizing AlPO-5 with hexagonal thin-plate morphology influenced by various parameters at ambient pressure. *Solid State Sci.* **2013**, *25*, 63–69. [CrossRef]

38. Ma, Y.-K.; Chia, S.; Paillaud, J.-L.; Daou, T.J.; Khoerunnisa, F.; El-Bahy, Z.M.; Ling, T.C.; Altalhi, A.A.; Mahmoud, S.F.; Ng, E.-P. SAPO-35 zeolite crystallized using novel structure-directing agent for catalytic conversion of levulinic acid into ethyl levulinate under non-microwave instant heating. *Mater. Chem. Phys.* **2022**, *287*, 126240. [CrossRef]

39. Wen, C.; Wang, X.; Xu, J.; Fan, Y. Hierarchical SAPO-11 molecular sieve-based catalysts for enhancing the double-branched hydroisomerization of alkanes. *Fuel* **2019**, *255*, 115821. [CrossRef]

40. Basina, G.; AlShami, D.; Polychronopoulou, K.; Tzitzios, V.; Balasubramanian, V.; Dawaymeh, F.; Karanikolos, G.N.; Al Wahedi, Y. Hierarchical $AlPO_4$-5 and SAPO-5 microporous molecular sieves with mesoporous connectivity for water sorption applications. *Surf. Coat. Technol.* **2018**, *353*, 378–386. [CrossRef]

41. Wang, X.; Guo, F.; Wei, X.; Liu, Z.; Zhang, W.; Guo, S.; Zhao, L. The catalytic performance of methylation of naphthalene with methanol over SAPO-11 zeolites synthesized with different Si content. *Korean J. Chem. Eng.* **2016**, *33*, 2034–2041. [CrossRef]

42. Morris, R.E. Ionothermal synthesis—Ionic liquids as functional solvents in the preparation of crystalline materials. *Chem. Commun.* **2009**, *21*, 2990–2998. [CrossRef] [PubMed]

43. Wang, Y.; Xu, Y.; Li, D.; Liu, H.; Li, X.; Tao, S.; Tian, Z. Ionothermal synthesis of zeolitic imidazolate frameworks and the synthesis dissolution-crystallization mechanism. *Chin. J. Catal.* **2015**, *36*, 855–865. [CrossRef]

44. Oh, H.-C.; Jung, S.; Ko, I.-J.; Choi, E.-Y. Ionothermal Synthesis of Metal-Organic Framework. In *Recent Advancements in the Metallurgical Engineering and Electrodeposition*; Al-Naib, U., Vikraman, D., Karuppasamy, K., Eds.; Intechopen: London, UK, 2020; pp. 1–24. [CrossRef]

45. Maton, C.; De Vos, N.; Stevens, C.V. Ionic liquid thermal stabilities: Decomposition mechanisms and analysis tools. *Chem. Soc. Rev.* **2013**, *42*, 5963–5977. [CrossRef] [PubMed]

46. Tosheva, L.; Ng, E.-P.; Mintova, S.; Hölzl, M.; Metzger, T.H.; Doyle, A.M. $AlPO_4$-18 Seed Layers and Films by Secondary Growth. *Chem. Mater.* **2008**, *20*, 5721–5726. [CrossRef]

47. Soulard, M.; Bilger, S.; Kessler, H.; Guth, J. Characterization of the products remaining in the solid after partial thermal decomposition of Pr4NF-, Pr3NHF-, and Pr4NOH-MFI precursors. *Zeolites* **1991**, *11*, 107–115. [CrossRef]

48. *The Molecular Sizes of the Compounds Were Estimated Using HyperChem™-Release 8.0 for Windows Molecular Modeling System*; Hypercube, Inc.: Gainesville, FL, USA, 2011.

49. Adam, F.; Kueh, C.-W.; Ng, E.-P. The immobilization of iron(III) aminopyridine complex on MCM-41: Its preparation and characterization. *J. Porous Mater.* **2013**, *20*, 1337–1343. [CrossRef]

50. Sing, K.S.W. Reporting physisorption data for gas/solid systems with special reference to the determination of surface area and porosity (Recommendations 1984). *Pure Appl. Chem.* **1985**, *57*, 603–619. [CrossRef]

51. Lima, G.C.C.S.; Mello, M.I.S.; Bieseki, L.; Araujo, A.S.; Pergher, S.B.C. Hydrothermal Synthesis of Silicoaluminophosphate with AEL Structure Using a Residue of Fluorescent Lamps as Starting Material. *Molecules* **2021**, *26*, 7366. [CrossRef]

52. Choo, M.-Y.; Oi, L.E.; Ling, T.C.; Ng, E.-P.; Lin, Y.-C.; Centi, G.; Juan, J.C. Deoxygenation of triolein to green diesel in the H2-free condition: Effect of transition metal oxide supported on zeolite Y. *J. Anal. Appl. Pyrolysis* **2020**, *147*, 104797. [CrossRef]

53. Shuit, S.H.; Ng, E.P.; Tan, S.H. A facile and acid-free approach towards the preparation of sulphonated multi-walled carbon nanotubes as a strong protonic acid catalyst for biodiesel production. *J. Taiwan Inst. Chem. Eng.* **2015**, *52*, 100–108. [CrossRef]

54. Alfonzo, M.; Goldwasser, J.; López, C.; Machado, F.; Matjushin, M.; Méndez, B.; de Agudelo, M.R. Effect of the synthesis conditions on the crystallinity and surface acidity of SAPO-11. *J. Mol. Catal. A Chem.* **1995**, *98*, 35–48. [CrossRef]

55. Du, R.-L.; Wu, K.; Xu, D.-A.; Chao, C.-Y.; Zhang, L.; Du, X.-D. A modified Arrhenius equation to predict the reaction rate constant of Anyuan pulverized-coal pyrolysis at different heating rates. *Fuel Process. Technol.* **2016**, *148*, 295–301. [CrossRef]

56. Ma, Y.-K.; Chia, S.; Daou, T.J.; Khoerunnisa, F.; El-Bahy, S.M.; El-Bahy, Z.M.; Ling, T.C.; Ng, E.-P. SAPO-34 crystallized using novel pyridinium template as highly active catalyst for synthesis of ethyl levulinate biofuel. *Microporous Mesoporous Mater.* **2022**, *333*, 111754. [CrossRef]

57. Kiss, A.A.; Dimian, A.C.; Rothenberg, G. Solid Acid Catalysts for Biodiesel Production —Towards Sustainable Energy. *Adv. Synth. Catal.* **2006**, *348*, 75–81. [CrossRef]

58. Song, W.; Zhao, C.; Lercher, J.A. Importance of Size and Distribution of Ni Nanoparticles for the Hydrodeoxygenation of Microalgae Oil. *Chem. A Eur. J.* **2013**, *19*, 9833–9842. [CrossRef]